Editors' Suggestion

Gate-tunable enhancement of supercurrent in hybrid planar Josephson junctions

Peng Yu,[1] Han Fu,[2,3] William F. Schiela,[1] William Strickland,[1] Bassel Heiba Elfeky,[1] S. M. Farzaneh,[1] Jacob Issokson,[1] Enrico Rossi,[2] and Javad Shabani[1]

[1]*Center for Quantum Information Physics, New York University, New York, New York 10003, USA*
[2]*Department of Physics, William & Mary, Williamsburg, Virginia 23187, USA*
[3]*Department of Physics, Florida Atlantic University, Boca Raton, Florida 33431, USA*

(Received 21 May 2024; accepted 16 July 2025; published 18 August 2025)

Planar Josephson junctions (JJs) have emerged as a promising platform for the realization of topological superconductivity and Majorana zero modes. To obtain robust quasi one-dimensional (1D) topological superconducting states using planar JJs, limiting the number of 1D Andreev bound states' subbands that can be present, and increasing the size of the topological superconducting gap are two fundamental challenges. It has been suggested that both problems can be addressed by properly designing the interfaces between the JJ's normal region and the superconducting leads. We fabricated Josephson junctions with periodic hole structures on the superconducting contact leads on InAs heterostructures with epitaxial superconducting Al. By depleting the chemical potential inside the holes region with a top gate, we observed an enhancement of the supercurrent across the junction. The theoretical analysis shows that the enhancement of the JJ's critical current is achieved when the depletion of the holes is such to optimize the matching of quasiparticles' wave function at the normal/superconductor interface. These results show how the combination of carefully designed patterns for the Al coverage, and external gates, can be successfully used to tune the density and wave functions' profiles in the normal region of the JJ, and therefore open an avenue to tune some of the critical properties, such as number of subbands and size of the topological gap, that must be optimized to obtain robust quasi-1D superconducting states supporting Majorana bound states.

DOI: 10.1103/3ccp-qyqs

Planar Josephson junctions based on 2DEGs with spin-orbit coupling have attracted a lot of attention in recent years, due to their potential to realize topological superconductivity and Majorana zero modes (MZM) [1–6]. In the presence of a Zeeman field, the normal region in the Josephson junction can host Majorana zero modes at its ends [7,8]. While solid progress has been made in both planar Josephson junctions and hybrid nanowire systems toward the realization of MZM [9–16], so far an unambiguous demonstration of MZM is still missing [17–20]. More evidence indicates that in hybrid systems there is a competition between disorder and the topological gap [21,22]. As spin-orbit coupling and induced gaps jointly determine the size of the topological gap at finite magnetic fields [23], an ideal hybrid system should have strong spin-orbit coupling and a large induced gap [24,25].

Several theoretical proposals suggest modification of the Josephson junction geometry could lead to an enhanced induced gap and even an enhanced Rashba spin-orbit coupling [2,26,27]. To realize a robust topological superconducting state in planar JJs, it is important to maintain the carrier density in the normal region (N) of the junction as low as possible. With this constraint, one could consider increasing the JJ's critical current by tuning the doping of the superconducting leads. In JJs with a normal design this cannot be done via external gates given the strong screening of the superconducting material. However, by creating holes along a strip in the superconducting coverage of the semiconductor it is possible to achieve two, seemingly contrasting, results: (i) tuning of the carrier density in a strip close to N; (ii) preservation of the overall superconducting phase coherence in the superconducting lead across the strip (via the regions between the holes). In this work we present experimental and theoretical results for JJs designed to maximize the critical current while keeping the doping in N fixed.

We fabricated Josephson junctions on epitaxial superconducting Al thin films grown *in situ* on InAs heterostructures. Such devices have shown high transparency [28–31] and a spin-orbit induced anomalous phase [32]. The Josephson junction is 4 μm long with a width of around 100 nm. Two rows of periodic holes are etched on each side of the Al contacts as shown in Fig. 1(a). Each hole is approximately 110 nm wide and 220 nm long. To control the chemical potential in the junction as well as in the holes region, we fabricated two layers of gates. In the first layer, a junction gate (JG) that covers the middle section of the junction is used to control the chemical potential in the junction. In the second layer, which is separated from the first gate by a second layer of dielectric, a top gate (TG) covers a much larger device region that includes the holes and the ends of the junction. A schematic diagram of the device and the material stacks are presented in Figs. 1(a) and 1(b). As shown in Fig. 1(a), the JG is shorter than the junction by 100 nm at each end by design. Although JG itself cannot fully deplete the junction, as it does not cover the ends of the junction, the chemical potential in the whole junction can still be fully controlled by using JG and TG together (see the SM [33]). We notice that TG depletes the ends of the junction around −2.5 V (see the SM [33]). Since the 2DEG inside the holes region should have a similar

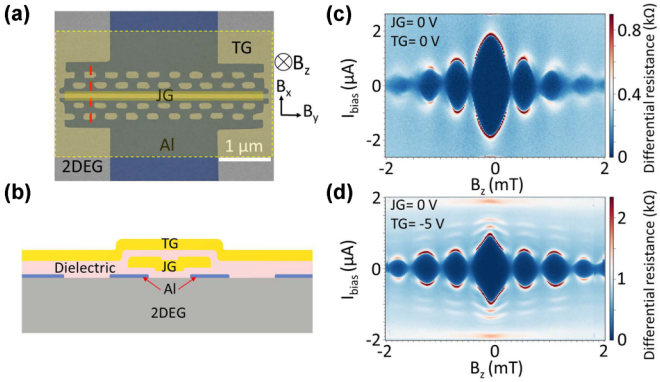

FIG. 1. (a) False-color scanning electron micrograph of the measured device. (b) Schematic of the device and the material stacks. (c), (d) Differential resistance as a function of the bias current and out-of-plane magnetic field for JG = 0 V and TG = 0 V (c) and JG = 0 V and TG = −5 V (d).

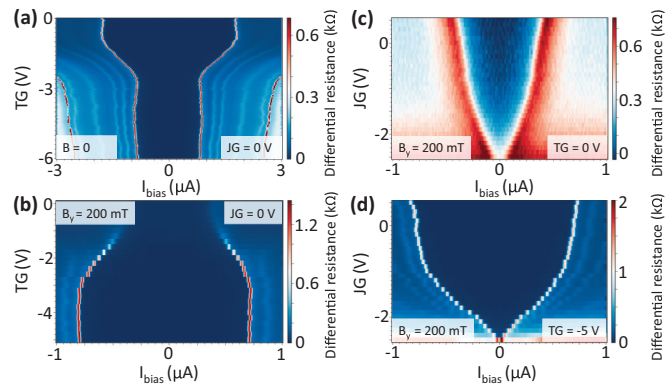

FIG. 2. Differential resistance as a function of the bias current and TG voltages at zero magnetic field (a) and $B_y = 200$ mT (b). Differential resistance as a function of the bias current and JG voltages at $B_y = 200$ mT when TG = 0 V (c) and TG = −5 V (d).

density and coupling to TG as the 2DEG in the junction, we expect that the 2DEG in the holes region should also be depleted around TG = −2.5 V. Tuning the chemical potential of the 2DEG in the holes region has a nontrivial effect on the junction, as discussed below. All measurements in this study were performed in a dilution refrigerator equipped with a three-axis vector magnet (see the SM [33]). As shown in Fig. 1(a), the z axis of the magnet is perpendicular to the device plane, while x and y axes are in-plane fields aligned parallel and perpendicular to the current, respectively. Differential resistance is measured using standard low-frequency lock-in techniques in a four-point manner (see the SM [33]). In Figs. 1(c) and 1(d), we present differential resistance as a function of the bias current and applied out-of-plane magnetic field for two different gate configurations. We find that the critical current is larger when the current is swept from zero to high bias than vice versa. This is most likely due to heating (see the SM [33]). To avoid artifacts due to such a hysteresis effect, all the results presented were taken with the bias swept from high bias to zero unless otherwise specified (see the SM [33]). All gates are set to 0 for Fig. 1(c). In Fig. 1(d), TG is set to −5 V while JG remains at 0. As TG is below −2.5 V in Fig. 1(d), the holes region is supposed to be depleted. The periodicity of the Fraunhofer patterns reveals an effective junction area of approximately 4.6 μm^2, which is larger than the nominal junction area of 0.4 μm^2 due to flux focusing caused by the Meissner effect and London penetration [34,35]. The peculiar triangular shape of the central lobe is due to a fraction of the supercurrent flowing just outside the edges of the JJ [33]. Overall, the two Fraunhofer patterns show similar periodicity, suggesting the effective junction area is not significantly modified by the depletion of the holes region. Next, we characterize the supercurrent gate dependence at different magnetic fields. At zero field, the supercurrent decreases when the voltage on TG is swept from 0 to −2.5 V as a result of depletion of the ends of the junction [Fig. 2(a)]. Below TG = −2.5 V, however, the supercurrent remains almost unchanged since the middle section of the junction is inaccessible by the TG due to the screening of the JG. For JG, the dependence is simpler, as the supercurrent always decreases monotonically with a decreasing JG voltage (see the SM [33]). When the magnetic field is turned on, the supercurrent shows a very different behavior regarding TG voltages. At $B_y = 200$ mT, where B_y is perpendicular to the supercurrent, the supercurrent is significantly enhanced when a more negative voltage is applied to the TG [Fig. 2(b)]. The supercurrent reaches its maximum around TG = −2.5 V and remains almost constant for TG voltages below that value. The presence of an in-plane component of the magnetic field can significantly modify the spatial profile of the supercurrent. In this scenario the maximum value of the critical current (I_c) as a function of the perpendicular component of the magnetic field is expected to shift from zero to a finite value of B_z [36]. As we show in detail in the SM [33], however, we find that in our JJs the maximum value of I_c as a function of B_z is always found at $B_z = 0$ (within the accuracy of our setup). In particular this is the case for $B_y = 200$ mT, the value of B_y for which we observe a strong enhancement of I_c as a function of TG. This suggests that a redistribution of the supercurrent profile is unlikely to be the reason for the observed enhancement of I_c as the holes are depleted. For fields parallel to the supercurrent, we observed a similar enhancement of the supercurrent with TG voltages (see the SM [33]). When TG is fixed to 0 V and −5 V and $B_y = 200$ mT, sweeping JG reveals that the supercurrent still monotonically decreases with decreasing JG voltages Figs. 2(c) and 2(d). That indicates that the enhancement of supercurrent is solely determined by the change of the chemical potential in the holes region and is not related to the change of the chemical potential in the junction.

The enhancement of the supercurrent can also be observed in in-plane magnetic field scans when the gate voltages are fixed. In Fig. 3(a), we plot differential resistance as a function of B_y and bias current for TG = 0 V and JG = 0 V. The supercurrent exhibits a nonlinear behavior as it first quickly decreases at low fields followed by a much slower decline at higher fields. When TG is fixed to −5 V, Fig. 3(b), the supercurrent has an almost linear dependence on B_y. From $B_y = 0.1$ T to $B_y = 0.5$ T, the supercurrent still preserves 40% of its value.

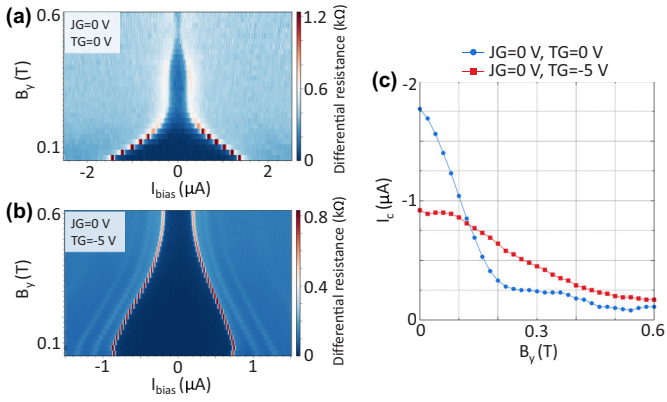

FIG. 3. Differential resistance as a function of the bias current and B_y when JG $= 0$ V, TG $= 0$ V (a) and JG $= 0$ V, TG $= -5$ V (b). (c) Critical currents as a function of B_y for TG $= 0$ and TG $= -5$ V extracted from bias current vs TG scans at different in-plane fields.

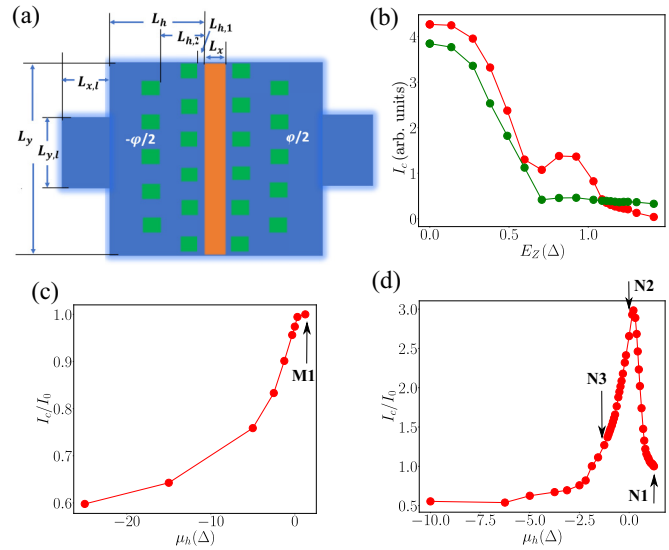

FIG. 4. (a) Schematic of simulation setup to model the experiments. (b) I_c as a function of E_Z for $\mu_h = \mu = 1.25\Delta$ (red) and $\mu_h = -1.25\Delta$ (green). (c), (d) I_c vs μ_h for $E_Z = 0$ and $E_Z = 1.14\Delta$, respectively. In (c) and (d) I_0 is the value of I_c when $\mu_h = \mu$.

In Fig. 3(c), we plot I_c as a function of B_y for TG $= 0$ and TG $= -5$ V extracted from bias current vs TG scans at different in-plane fields. As can be seen, the two critical currents cross around $B_y = 0.12$ T, confirming the observation that the enhancement of the supercurrent occurs only at finite fields and when the voltage on TG is below the specific value. In another device, we have observed a similar enhancement of supercurrent at finite fields when TG is below a certain value (see the SM [33]).

To understand the origin of this dependence of critical currents on the gate voltage, we set up a tight-binding model for the Boguliobov de Gennes (BdG) Hamiltonian describing the system (see the SM [33]), using the python package Kwant [37]. To be able to obtain from the model all the desired quantities, in particular the critical current, with the available computational resources, we scaled down all the dimensions while using a value of the superconducting gap Δ and of the chemical potential μ in the regions outside the holes such that the ratio between the geometric dimensions and the superconducting coherence length, ξ, is of the same order as in the experiment. For the results presented below we use a value of Δ 16 times larger than the physical one and set $\mu = 1.25\Delta$. The geometry of the model used is shown in Fig. 4(a). To properly model the superconducting leads we chose a value of $L_{x,l}$ sufficiently larger than ξ to avoid spurious finite-size effects.

We first obtain the ABSs's spectrum $\{\epsilon_n(\varphi)\}$ as a function of the phase difference φ between the superconducting pairing of the two leads. We then calculate the supercurrent $I(\varphi) = \sum_{\epsilon_n<0}(\partial\epsilon_n/\partial\varphi)(2\pi/\Phi_0)$, where $\Phi_0 = h/2e$ is the magnetic flux quantum. From this, the critical current $I_c = \max(I(\varphi))$ is extracted for different values of the in-plane magnetic field and chemical potential μ_h of the holes.

Figure 4(b) shows the evolution of I_c with the strength of the Zeeman energy E_Z due to an in-plane magnetic field perpendicular to the current for the case when $\mu_h = \mu$, in red, and $\mu_h = -1.25\Delta$, in green. The Zeeman energy in the superconductor is taken to be $1/2$ the value in the normal and depleted regions. In the first case the holes are normal regions, i.e., regions where Δ is set to zero, with the same carrier density as the rest of the system. In the second case the carrier density in the holes is lower than in the areas around them. In both cases we see that I_c first decreases with E_Z up to $E_Z \approx 0.6\Delta$. For $E_z > 0.6\Delta$ in the first case I_c changes nonmonotonically with E_Z, a behavior that can be attributed to the almost closing and reopening of the gap of the ABS's spectrum In the second case I_c keeps decreasing also for $E_z > 0.6\Delta$, albeit more slowly, suggesting that in this case the gap of the ABS doesn't recover with E_Z.

As in the experimental case, from Fig. 4(b), we see that above a threshold value of E_Z, $E_Z \approx 1.1\Delta$, I_c for the depleted case is larger than for the nondepleted, suggesting that for $E_Z > 1.1\Delta$ the evolution of I_c with μ_h might be not monotonic. This is confirmed by the results for the evolution of I_c with respect to μ_h shown in Figs. 4(c) and 4(d), for the $E_Z = 0$ and $E_Z = 1.14\Delta$ cases, respectively. We see that for $E_Z = 0$, I_c decreases monotonically as the depletion $(-\mu_h)$ of the holes increases, whereas for $E_Z = 1.14\Delta$, I_c varies nonmonotonically with μ_h, in qualitative agreement with the experimental results.

We have verified, see the SM [33], that different values of the spin-orbit coupling (SOC) strength, and different directions of the in-plane magnetic field do not modify qualitatively the results presented in Figs. 4(b)–4(d).

Figure 5 shows the spatial profile of the quasiparticle current density $J_x(x, y) = -i(\hbar/2m^*)\sum_{\epsilon_n<0}(\psi_n^*\nabla\psi_n - \psi_n\nabla\psi_n^*)$ [38], where ψ_n are the eigenstates of the BdG Hamiltonian and m^* is the effective mass. Notice that the regions where $J = 0$ are regions where the current is carried by the superconducting condensate. Panels (a) and (b) show the results for the case $E_Z = 1.14\Delta$ for the values of μ_h denoted by $N1$, $N2$ in Fig. 4(d). We see that for the value of μ_h for which I_c is maximum, panel (b), J is more uniform in the central region of the JJ. This suggests that the optimal value of μ_h results in a better matching of the quasiparticle wave functions across the different regions of the JJ.

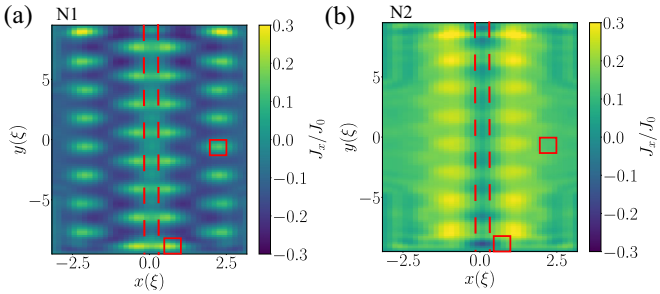

FIG. 5. (a), (b) Profile of J_x for the case when $E_Z = 1.14\Delta$ and μ_h corresponds to the points N1, N2 in Fig. 4(d), respectively. J_0 is the average current density for the case when $E_Z = 0$, $\mu_h = \mu$. The red dashed lines indicate the boundary of the normal strip. The red boxes show positions of some of the depleted holes.

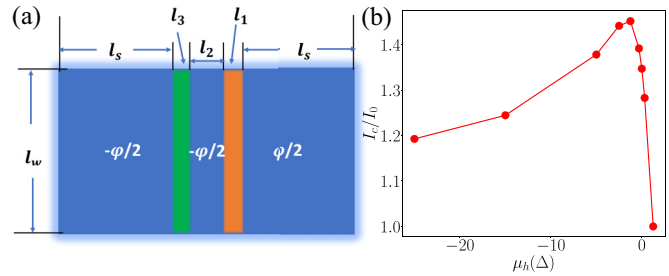

FIG. 6. (a) Layout of simplified two-strip model. (b) Scaling of I_c with μ_h obtained using the simplified model for the case when $l_2 = \xi/2$, $E_Z = 0$, SOC $= 0$. $I_0 = I_c(\mu_h = \mu)$.

To check that this is the case, we considered a simplified model, shown in Fig. 6(a). In this model the holes are effectively replaced by a normal strip, shown in green in Fig. 6(a), at a distance l_2 from the normal region of the JJ. Notice that the difference of the superconducting phase across the normal region modeling the holes is set to zero. This is done to take into account that in the experimental geometry there are paths between the holes that connect the different superconducting regions on the same side of the JJ's normal region, the region shown in orange in Fig. 6(a), that separates the left and right superconducting leads.

Using the simplified model we were able to see that the critical parameter determining the nature of the evolution of I_c with respect to μ_h is the distance l_2 between the normal region modeling the holes, the depletion strip, and the JJ's normal region. We find that when $l_2 \ll \xi$, I_c decreases monotonically with $(-\mu_h)$, while at $l_2 \sim \xi$, I_c varies nonmonotonically with $(-\mu_h)$ as shown in Fig. 6(b). For $l_2 \gg \xi$ the two normal strips are effectively decoupled from each other and so μ_h has no effect on I_c. These results suggest that the main reason why experimentally a nonmonotonic scaling of I_c vs $(-\mu_h)$ is observed in the presence of an in-plane magnetic field is the fact that when $E_Z \gtrsim \Delta$ the ABSs' wave functions decay faster in the superconducting regions at the sides of the JJ's normal region, effect that in the simplified model corresponds to a reduction of ξ [39] and therefore to an increase of the ratio l_2/ξ to values ~ 1 for which I_c scales nonmonotonically with μ_h.

To further understand the origin of the observed dependence of I_c on l_2/ξ and μ_h we calculated the reflection coefficients of a superconducting-normal (SN) junction with a depletion region on the superconducting side at a distance l_2 from the SN interface. We found, see Fig. S10 in the SM [33], that the depletion of the holes, equivalent in the simplified model to the depletion of the green strip in Fig. 6(a), can be tuned to maximize the value of the electrons' wavefunction at the boundary between the superconducting lead and JJ's normal region, and so optimize the ratio $|r_A/r_N|$ between Andreev reflection, r_A, and normal reflection, r_N, and therefore the JJ's critical current I_c, when $l_2 = \xi/2$. We therefore conclude that varying via an external gate the depletion of the holes for a JJ like the one shown in Fig. 1(a) results in the effective tuning of the spatial profile of the quasiparticles wave functions leading to qualitative changes of critical properties such as the JJ's critical current.

In summary, we have fabricated Josephson junctions with periodic hole structures on the Al contact. A counterintuitive enhancement of supercurrent has been observed when the 2DEG in the holes region is depleted by the TG. Theoretical modeling and careful analysis of the experimental results show that such unusual enhancement of the critical current is due to changes of the spatial profile of the quasiparticles' wave functions. The ability to shape and engineer the wave function of the electronic quantum states is critical to realize robust topological superconducting states supporting non-Abelian quasiparticles. Our results show that by combining specific Al coverage layouts in InAs/Al planar JJs with external gates, a unique control of the profile of the electrons' wave functions can be achieved, resulting in remarkable tunability of key properties of the JJs.

This project was funded by the U.S. Department of Energy, Office of Basic Energy Sciences, via Award No. DE-SC0022245. H.F. and E.R. thank Joseph J. Cuozzo for very helpful discussions during the initial stages of the work.

W.S. grew the material heterostructure. P.Y. fabricated the devices. P.Y. with the help of W.F.S., B.H.E, and S.M.F. performed the measurements. H.F. and E.R. developed the theoretical description and obtained the theoretical results. P.Y., H.F., E.R., and J.S. analyzed the results and wrote the manuscript with contributions from all of the authors.

[1] F. Setiawan, A. Stern, and E. Berg, Topological superconductivity in planar Josephson junctions: Narrowing down to the nanowire limit, Phys. Rev. B **99**, 220506(R) (2019).

[2] A. Melo, S. Rubbert, and A. R. Akhmerov, Supercurrent-induced Majorana bound states in a planar geometry, SciPost Phys. **7**, 039 (2019).

[3] O. Lesser, A. Saydjari, M. Wesson, A. Yacoby, and Y. Oreg, Phase-induced topological superconductivity in a planar heterostructure, Proc. Natl. Acad. Sci. USA **118**, e2107377118 (2021).

[4] N. Mohanta, S. Okamoto, and E. Dagotto, Skyrmion control of Majorana states in planar Josephson junctions, Commun. Phys. **4**, 163 (2021).

[5] C. Peng, A. Haim, T. Karzig, Y. Peng, and G. Refael, Floquet Majorana bound states in voltage-biased planar Josephson junctions, Phys. Rev. Res. **3**, 023108 (2021).

[6] A. Banerjee, O. Lesser, M. A. Rahman, H.-R. Wang, M.-R. Li, A. Kringhøj, A. M. Whiticar, A. C. C. Drachmann, C. Thomas, T. Wang, M. J. Manfra, E. Berg, Y. Oreg, A. Stern, and C. M. Marcus, Signatures of a topological phase transition in a planar Josephson junction, Phys. Rev. B **107**, 245304 (2023).

[7] M. Hell, M. Leijnse, and K. Flensberg, Two-dimensional platform for networks of Majorana bound states, Phys. Rev. Lett. **118**, 107701 (2017).

[8] F. Pientka, A. Keselman, E. Berg, A. Yacoby, A. Stern, and B. I. Halperin, Topological superconductivity in a planar Josephson junction, Phys. Rev. X **7**, 021032 (2017).

[9] V. Mourik, K. Zuo, S. M. Frolov, S. R. Plissard, E. P. A. M. Bakkers, and L. P. Kouwenhoven, Signatures of Majorana fermions in hybrid superconductor-semiconductor nanowire devices, Science **336**, 1003 (2012).

[10] M. T. Deng, S. Vaitiekenas, E. B. Hansen, J. Danon, M. Leijnse, K. Flensberg, J. Nygård, P. Krogstrup, and C. M. Marcus, Majorana bound state in a coupled quantum-dot hybrid-nanowire system, Science **354**, 1557 (2016).

[11] J. Chen, P. Yu, J. Stenger, M. Hocevar, D. Car, S. R. Plissard, E. P. A. M. Bakkers, T. D. Stanescu, and S. M. Frolov, Experimental phase diagram of zero-bias conductance peaks in superconductor/semiconductor nanowire devices, Sci. Adv. **3**, e1701476 (2017).

[12] J. Shabani, M. Kjaergaard, H. J. Suominen, Y. Kim, F. Nichele, K. Pakrouski, T. Stankevic, R. M. Lutchyn, P. Krogstrup, R. Feidenhans'l, S. Kraemer, C. Nayak, M. Troyer, C. M. Marcus, and C. J. Palmstrøm, Two-dimensional epitaxial superconductor-semiconductor heterostructures: A platform for topological superconducting networks, Phys. Rev. B **93**, 155402 (2016).

[13] H. Ren, F. Pientka, S. Hart, A. T. Pierce, M. Kosowsky, L. Lunczer, R. Schlereth, B. Scharf, E. M. Hankiewicz, L. W. Molenkamp, B. I. Halperin, and A. Yacoby, Topological superconductivity in a phase-controlled Josephson junction, Nature (London) **569**, 93 (2019).

[14] A. Fornieri, A. M. Whiticar, F. Setiawan, E. Portolés, A. C. C. Drachmann, A. Keselman, S. Gronin, C. Thomas, T. Wang, R. Kallaher, G. C. Gardner, E. Berg, M. J. Manfra, A. Stern, C. M. Marcus, and F. Nichele, Evidence of topological superconductivity in planar Josephson junctions, Nature (London) **569**, 89 (2019).

[15] M. C. Dartiailh, W. Mayer, J. Yuan, K. S. Wickramasinghe, A. Matos-Abiague, I. Žutić, and J. Shabani, Phase signature of topological transition in Josephson junctions, Phys. Rev. Lett. **126**, 036802 (2021).

[16] D.-X. Qu, J. J. Cuozzo, N. E. Teslich, K. G. Ray, Z. Dai, T. T. Li, G. F. Chapline, J. L. DuBois, and E. Rossi, Phase-slip lines and anomalous Josephson effects in tungsten nanoscale cluster-based topological insulator nanobridges: Implications for topologically protected qubits and quantum sensors, ACS Appl. Nano Mater. **7**, 3702 (2024).

[17] S. Das Sarma and H. Pan, Disorder-induced zero-bias peaks in Majorana nanowires, Phys. Rev. B **103**, 195158 (2021).

[18] P. Yu, J. Chen, M. Gomanko, G. Badawy, E. P. A. M. Bakkers, K. Zuo, V. Mourik, and S. M. Frolov, Non-Majorana states yield nearly quantized conductance in proximatized nanowires, Nat. Phys. **17**, 482 (2021).

[19] H. Pan and S. Das Sarma, Physical mechanisms for zero-bias conductance peaks in Majorana nanowires, Phys. Rev. Res. **2**, 013377 (2020).

[20] J. Chen, B. Woods, P. Yu, M. Hocevar, D. Car, S. Plissard, E. Bakkers, T. Stanescu, and S. Frolov, Ubiquitous non-Majorana zero-bias conductance peaks in nanowire devices, Phys. Rev. Lett. **123**, 107703 (2019).

[21] S. Ahn, H. Pan, B. Woods, T. D. Stanescu, and S. Das Sarma, Estimating disorder and its adverse effects in semiconductor Majorana nanowires, Phys. Rev. Mater. **5**, 124602 (2021).

[22] P. Yu, B. D. Woods, J. Chen, G. Badawy, E. P. A. M. Bakkers, T. D. Stanescu, and S. M. Frolov, Delocalized states in three-terminal superconductor-semiconductor nanowire devices, SciPost Phys. **15**, 005 (2023).

[23] T. D. Stanescu, R. M. Lutchyn, and S. Das Sarma, Majorana fermions in semiconductor nanowires, Phys. Rev. B **84**, 144522 (2011).

[24] M. Pendharkar, B. Zhang, H. Wu, A. Zarassi, P. Zhang, C. P. Dempsey, J. S. Lee, S. D. Harrington, G. Badawy, S. Gazibegovic, R. L. M. O. het Veld, M. Rossi, J. Jung, A.-H. Chen, M. A. Verheijen, M. Hocevar, E. P. A. M. Bakkers, C. J. Palmstrøm, and S. M. Frolov, Parity-preserving and magnetic field–resilient superconductivity in InSb nanowires with Sn shells, Science **372**, 508 (2021).

[25] T. Kanne, M. Marnauza, D. Olsteins, D. J. Carrad, J. E. Sestoft, J. de Bruijckere, L. Zeng, E. Johnson, E. Olsson, K. Grove-Rasmussen, and J. Nygård, Epitaxial Pb on InAs nanowires for quantum devices, Nat. Nanotechnol. **16**, 776 (2021).

[26] T. Laeven, B. Nijholt, M. Wimmer, and A. R. Akhmerov, Enhanced proximity effect in zigzag-shaped Majorana Josephson junctions, Phys. Rev. Lett. **125**, 086802 (2020).

[27] P. P. Paudel, T. Cole, B. D. Woods, and T. D. Stanescu, Enhanced topological superconductivity in spatially modulated planar Josephson junctions, Phys. Rev. B **104**, 155428 (2021).

[28] W. Mayer, J. Yuan, K. S. Wickramasinghe, T. Nguyen, M. C. Dartiailh, and J. Shabani, Superconducting proximity effect in epitaxial Al-InAs heterostructures, Appl. Phys. Lett. **114**, 103104 (2019).

[29] M. Kjaergaard, H. Suominen, M. Nowak, A. Akhmerov, J. Shabani, C. Palmstrøm, F. Nichele, and C. Marcus, Transparent semiconductor-superconductor interface and induced gap in an epitaxial heterostructure Josephson junction, Phys. Rev. Appl. **7**, 034029 (2017).

[30] M. C. Dartiailh, J. J. Cuozzo, B. H. Elfeky, W. Mayer, J. Yuan, K. S. Wickramasinghe, E. Rossi, and J. Shabani, Missing Shapiro steps in topologically trivial Josephson junction on InAs quantum well, Nat. Commun. **12**, 78 (2021).

[31] B. H. Elfeky, J. J. Cuozzo, N. Lotfizadeh, W. F. Schiela, S. M. Farzaneh, W. M. Strickland, D. Langone, E. Rossi, and J. Shabani, Evolution of 4π-periodic supercurrent in the presence of an in-plane magnetic field, ACS Nano **17**, 4650 (2023).

[32] W. Mayer, M. C. Dartiailh, J. Yuan, K. S. Wickramasinghe, E. Rossi, and J. Shabani, Gate controlled anomalous phase shift in Al/InAs Josephson junctions, Nat. Commun. **11**, 212 (2020).

[33] See Supplemental Material at http://link.aps.org/supplemental/10.1103/3ccp-qyqs for more details about device fabrication and measurement.

[34] B. H. Elfeky, N. Lotfizadeh, W. F. Schiela, W. M. Strickland, M. Dartiailh, K. Sardashti, M. Hatefipour, P. Yu, N. Pankratova, H. Lee, V. E. Manucharyan, and J. Shabani, Local control of supercurrent density in epitaxial planar Josephson junctions, Nano Lett. **21**, 8274 (2021).

[35] A. Paghi, L. Borgongino, S. Battisti, S. Tortorella, G. Trupiano, G. D. Simoni, E. Strambini, L. Sorba, and F. Giazotto, Josephson field effect transistors with InAs on insulator and high permittivity gate dielectrics, arXiv:2412.16221 [cond-mat.supr-con].

[36] T. Dvir, A. Zalic, E. H. Fyhn, M. Amundsen, T. Taniguchi, K. Watanabe, J. Linder, and H. Steinberg, Planar graphene-$NbSe_2$ Josephson junctions in a parallel magnetic field, Phys. Rev. B **103**, 115401 (2021).

[37] C. W. Groth, M. Wimmer, A. R. Akhmerov, and X. Waintal, Kwant: a software package for quantum transport, New J. Phys. **16**, 063065 (2014).

[38] C. W. J. Beenakker, Three "universal" mesoscopic Josephson effects, in *Transport Phenomena in Mesoscopic Systems*, edited by H. Fukuyama and T. Ando (Springer, Berlin, Heidelberg, 1992), pp. 235–253.

[39] In reality, the magnetic field will also suppress the superconducting gap. However, for the magnetic field considered, such effect is much smaller than the one arising from the reduction of the decay length of the ABS states.

Supplemental Material: Gate tunable enhancement of supercurrent in hybrid planar Josephson junctions

Peng Yu,[1] Han Fu,[2,3] William F. Schiela,[1] William Strickland,[1] Bassel Heiba Elfeky,[1] S. M. Farzaneh,[1] Jacob Issokson,[1] Enrico Rossi,[2] and Javad Shabani[1]

[1] *Center for Quantum Information Physics, New York University, New York, NY 10003, USA*
[2] *Department of Physics, William & Mary, Williamsburg, Virginia 23187, USA*
[3] *Department of Physics, Florida Atlantic University, Boca Raton, Florida, 33431, USA*

(Dated: July 17, 2025)

EXPERIMENTAL DETAILS

Methods— Wafers are grown by molecular beam epitaxy. Devices are fabricated using a combination of wet etching and deposition techniques after electron beam lithography. Device mesa features are defined by a deep wet etch with 85% concentrated phosphoric acid, 30% concentrated hydrogen peroxide, and deionized water in a volumetric ratio of 1:1:40 after selectively etching the aluminum top layer with Transene Aluminum Etchant Type D. Junction weak links and smaller device features are defined by a subsequent aluminum etch. Double-layer gates subsequently undergo two cycles of dielectric deposition of aluminum oxide via atomic layer deposition, and titanium/gold gates are deposited via electron beam evaporation. Measurements are performed in a dilution refrigerator at a temperature of around 30 mK using standard low-frequency lock-in amplification techniques with excitation currents of at most 10 nA and frequencies of around 17 and 77 Hz. The magnetic field is generated by a three-axis superconducting vector magnet. To align an in-plane field, B_y for example, with the device, we first take a series of out-of-plane field scans at different B_y (50 mT to 200 mT with an interval of 50 mT). Then based on the shift of Fraunhofer patterns at each in-plane field, we make an adjustment to the out-of-plane field to cancel the perpendicular component from B_y. In Fig.3(b) and (c), we only show B_y above 80 mT because of the difficulty in reliably calibrating the in-plane fields when B_y is less than 50 mT. Only when the in-plane field is above 50 mT can the field be aligned with a linear fit. To get an accurate switching current as a function of the in-plane field for all the field ranges, we first performed out-of-plane field scans at each in-plane field to align the field, and then extracted the switching current from bias current vs TG scans at each in-plane field as shown in Fig.3(a).

Experimental results— We show additional differential resistance plots at various values of the junction gate voltage, the top gate voltage, and the in-plane field in Fig. S1, Fig. S3. The Fraunhofer patterns for different gate settings at low in-plane fields are shown in Fig. S2 and Fig. S4, and Fraunhofer patterns at high in-plane fields are shown in Fig. S5. In Fig. S6, we present information related to the high supercurrent density at the ends of the junction. In Fig. S7, we demonstrate hysteresis in current-voltage characteristics and justify the use of a downward sweep direction. For a similar device (device B), the corresponding supercurrent dependence is given in Figs. S8 and S9.

Enlarged effective junction area— In the Josephson junction presented in the main text, we found an enlarged effective junction area of 4.6 μm^2 based on the periodicity of the Fraunhofer patterns, which is much larger than the nominal junction area of 0.4 μm^2 due to flux focusing caused by the Meissner effect and London penetration. Such an effect has been observed in similar Josephson junctions (Nano Lett. 2021, 21, 19, 8274–8280; arXiv:2412.16221). In the study of arXiv:2412.16221, the authors observe a similar increase in the effective junction area in InAs/Al Josephson junctions, consistent with our findings. They introduce a scaling factor (γ) to characterize the enhanced effective area for magnetic flux, which accounts for both magnetic field focusing and an increased junction length compared to the inter-electrode separation. Based on their analysis, γ is primarily determined by the ratio of the contact width (L_y) to the junction length (L_x). In our junctions, we also have a large L_y/L_x ratio, which naturally leads to the significantly enlarged effective junction area.

Effect and origin of the high supercurrent density at the ends of the junction— We performed supercurrent density reconstruction based on Fraunhofer patterns for $B_y = 0$ and JG = TG = 0 (Fig.s6(b)), which reveals a much higher supercurrent density at the ends of the junction. This kind of effect has been observed in similar InAs/Al Josephson junctions (Nano Lett. 2021, 21, 19, 8274–8280; arXiv:2412.16221). This high supercurrent density in our junctions could result from supercurrent flow outside the junction region due to the proximitized normal region between the junction ends and the additional Al contacts (red rectangular region in Fig.s6(a)). We acknowledge that alternative explanations exist (see arXiv:2412.16221 for a more detailed discussion). This effect offers a plausible explanation for why the TG-induced depletion of the junction ends can significantly alter the critical current as shown

in Fig.2(a). We can further demonstrate the effect of depleting the junction ends using data from our previous study (Nano Lett. 2021, 21, 19, 8274–8280). In that work, we employed five mini gates to control a 4 μm-long junction, where the two outer gates depleted the junction ends. When the ends were depleted, the high-density currents at the edges were suppressed, leading to a 50% reduction in the critical current at zero field. This 50% reduction in critical current due to the depletion of the ends is similar to what we observed in our manuscript when depleting the TG as shown in Fig.2(a). Furthermore, sweeping the in-plane field perpendicular to the supercurrent showed no enhancement of the critical current at finite fields when the ends were depleted. This data, therefore, serves as a control experiment, demonstrating that depleting the junction ends significantly reduces the critical current at zero field while not enhancing the critical current at finite fields.

Hysteresis in current-voltage characteristics and the choice of downward sweep direction— As shown in Fig.s7, we observed hysteresis in current-voltage characteristics when the bias is swept from positive to negative. For our Josephson junction, we calculated the McCumber parameter using $I_c = 1\ \mu A$, R_n=100 Ω, and C = $(\epsilon_r\epsilon_0 \mathrm{A})/\mathrm{d}$ = 35.4 fF with A = $4\mu m * 10nm$ (Al thickness), d = 100 nm.

$$\beta_C = \frac{2\pi I_c R_n^2 C}{\phi_0} \approx 0.00161$$

is much smaller than 1, which indicates a strongly overdamped junction and the hysteresis between the downward (retrapping current) and upward sweep critical currents is primarily due to the heating effect. Consequently, the retrapping current can be interpreted as the critical current measured at a slightly higher effective temperature. In practice, the choice of downward sweeps (retrapping current) over upward sweeps is mainly to reduce measurement time, as they require a lower current bias. Fig.s7(a)(b) can also justify the robustness of using the retrapping current. In these measurements, the positive branch corresponds to the retrapping current and is consistently smaller than the negative branch. In both plots, we observe that the retrapping current systematically varies with the gate voltages and follows the same trend as the negative branch. Since our study focuses on the gate dependence of the critical current and we exclusively use the retrapping current rather than comparing it to the upward sweep current, we believe that using the retrapping current does not compromise the robustness of our conclusions.

THEORETICAL ANALYSIS

Simulation details— In the simulations, the implemented Hamiltonian in the tight-binding model is the following for the normal metal (orange strip):

$$\begin{aligned} H_N = \sum_{i,j,\alpha,\beta} & \left[(4t-\mu)\tau_{z0} + E_Z\,\tau_{0y}\right]_{\alpha,\beta} c^\dagger_{i,j,\alpha} c_{i,j,\beta} + \Big\{ \left[-t\,\tau_{z0} - i\,l_{soc}\tau_{zy}\right]_{\alpha,\beta} c^\dagger_{i,j,\alpha} c_{i,j+1,\beta} \\ & + \left[-t\,\tau_{z0} + i\,l_{soc}\tau_{zx}\right]_{\alpha,\beta} c^\dagger_{i,j,\alpha} c_{i+1,j,\beta} + h.c. \Big\} \end{aligned} \tag{S1}$$

in the Nambu spinor basis. Here the position of the lattice is $(x, y) = (j, i)a$, a is the lattice constant, $\alpha, \beta = 1 - 4$ denote the spin and electron/hole degrees of freedom. $\tau_{m,n}$ means σ_m operator in the electron/hole sector, and σ_n in the spin degree of freedom, where σ_0 is the identity matrix and $\sigma_{x,y,z}$ is the usual Pauli matrix. $l_{soc} = \alpha_{soc}/2a$, α_{soc} is the Rashba SOC strength. E_Z represents the Zeeman term when we apply a magnetic field along the y direction. In our simulations, $t = 7.32\Delta, l_{soc} = 0.23\Delta$. In the depleted region (green), we have

$$\begin{aligned} H_h = \sum_{i,j,\alpha,\beta} & \left[(4t-\mu_h)\tau_{z0} + E_Z\,\tau_{0y}\right]_{\alpha,\beta} c^\dagger_{i,j,\alpha} c_{i,j,\beta} + \Big\{ \left[-t\,\tau_{z0} - i\,l_{soc}\tau_{zy}\right]_{\alpha,\beta} c^\dagger_{i,j,\alpha} c_{i,j+1,\beta} \\ & + \left[-t\,\tau_{z0} + i\,l_{soc}\tau_{zx}\right]_{\alpha,\beta} c^\dagger_{i,j,\alpha} c_{i+1,j,\beta} + h.c. \Big\} \end{aligned} \tag{S2}$$

with a different chemical potential μ_h. And in the superconductor, the Hamiltonian is

$$\begin{aligned} H_S = \sum_{i,j,\alpha,\beta} & \left[(4t-\mu)\tau_{z0} + g_{sc}\,E_Z\,\tau_{0y} + \Delta(\cos\phi\,\tau_{x0} - \sin\phi\,\tau_{y0})\right]_{\alpha,\beta} c^\dagger_{i,j,\alpha} c_{i,j,\beta} \\ & + \Big\{ \left[-t\,\tau_{z0} - i\,l_{soc}\tau_{zy}\right]_{\alpha,\beta} c^\dagger_{i,j,\alpha} c_{i,j+1,\beta} + \left[-t\,\tau_{z0} + i\,l_{soc}\tau_{zx}\right]_{\alpha,\beta} c^\dagger_{i,j,\alpha} c_{i+1,j,\beta} + h.c. \Big\} \end{aligned} \tag{S3}$$

where the superconductor pairing gap is $\Delta e^{i\phi}$, the phase $\phi = -\varphi/2$ in superconductors to left of the normal strip, and $\varphi/2$ on the right. g_{sc} represents the ratio between the g-factor in superconductors and that of the normal metal.

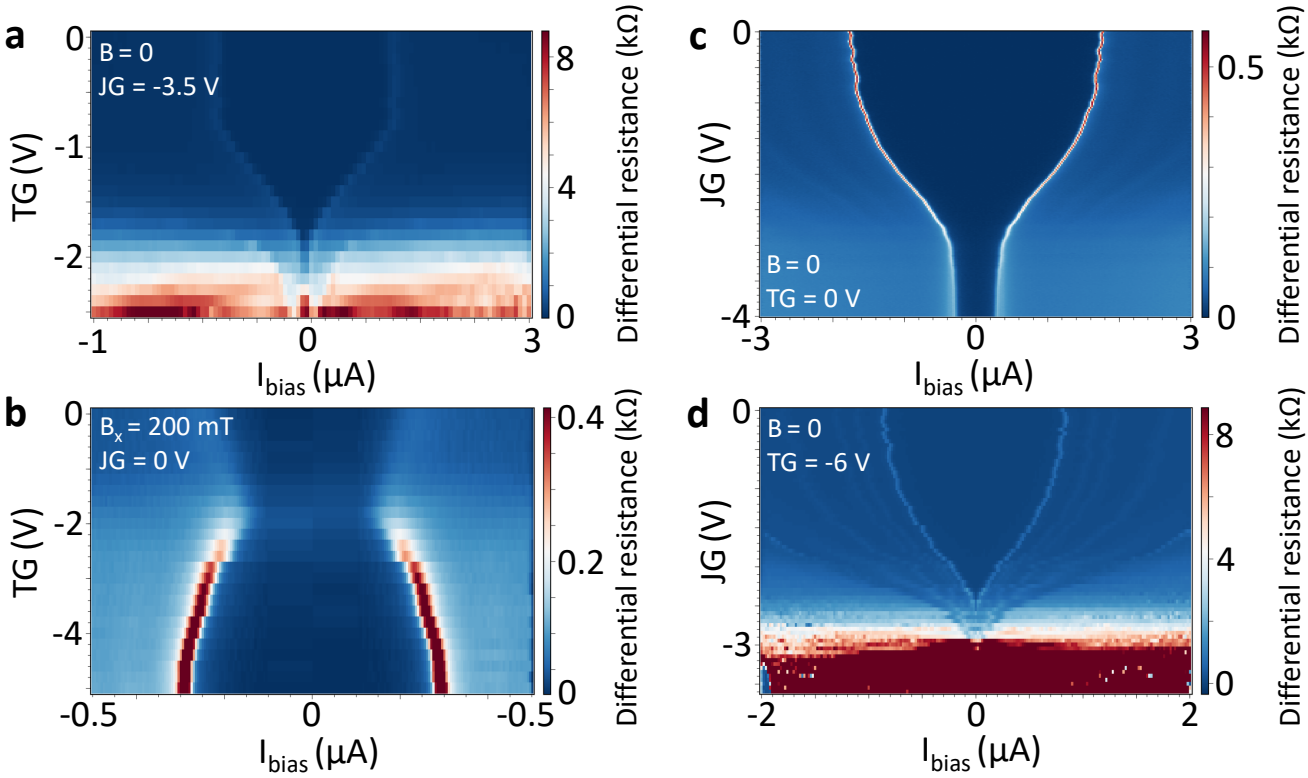

Fig S1. **Supercurrent gate dependence at zero field and in-plane fields parallel to the supercurrent.** (a) Differential resistance as a function of bias current and TG voltage at zero field and JG = -3.5 V. (b) Differential resistance as a function of bias current and TG voltage at $B_x = 200$ mT and JG = 0, supercurrent is enhanced when TG is below -2 V. (c) Differential resistance as a function of bias current and JG voltage at zero field and TG = 0 V. JG can not fully pinch off the supercurrent since it doesn't cover the ends of the junction and supercurrent can flow across the junction there. (d) Differential resistance as a function of bias current and JG voltage at zero field and TG = -6 V. JG can fully pinch off the supercurrent when the ends of the junction are depleted by the TG.

Here We choose $g_{sc} = 1/2$ in the simulations [1]. To avoid spurious finite size effects, the theoretical calculation of the spectrum of the Andreev bound states, requires superconducting leads of length $L_{sc} \gg \xi$. Given that for the systems considered $\xi \sim 400$ nm, and the width ~ 4 microns, the requirement $L_{sc} \gg \xi$ makes a full-scale calculation very expensive and beyond the capabilities of the computational resources that we can access. For this reason, we rescale down all our length-scales keeping, however, the ratios between all the different lengths the same as in the experiment. To achieve this rescaling, for the simulations we use $\Delta_{sc} = 3.68$ meV, so that the effective $\xi = \hbar v_f/\Delta_{sc} = 42$ nm, is much smaller. We then set $L_{sc}(= L_h + L_{x,l}) \sim 8\,\xi$, and make the ratios between all the other lengths and ξ as close as possible to the experimental values. To be more specific, in the punched hole setup, in the unit of coherence length ξ, the system sizes are $L_x = 0.5, L_{h,1} = 0.17, L_{h,2} = 1.67, L_h = 3, L_{x,l} = 4.67, L_{y,l} = 9.5, L_y = 19.17$. The hole has a horizontal width $L_{x,h} = 0.5$ and a vertical width $L_{y,h} = 1.17$. In the two-strip setup, the parameters are $l_1 = l_3 = 0.5\xi$, $l_s = 7.17\xi$, $l_w = 1.83\xi$. The lattice constant a in both setups is taken as $\xi/6$. In all our simulations, we include a total of 800 energy bands for the calculation of the supercurrent.

Numerical results—In Fig. S10, we show the energy spectrum and current-phase relation corresponding to points N1, N2, N3 in Fig. 4(d). For $\mu_h \sim \mu$ we have many ABSs (subbands) that give opposite contributions to the current I resulting in a small I_c. As μ_h is decreased to 0, some of the subbands are pushed to higher energies (and flattened) and so we have less of a cancellation and an increase of I_c. For even larger $(-\mu_h)$ the junctions become much less transparent, all the bands flatten, and so I_c decreases. In Fig. S11, we show the current distribution corresponding to M1 points in Fig. 4(c) and N1, N2, N3 in Fig. 4(d). Panel (a) shows the profile of J for the case when $E_Z = 0$. We see that the presence of the holes induces a periodic modulation in the transverse direction of the current in the normal region of the JJ. In Fig. S12, we show that in the punched-hole structure, the SOC strength and the direction

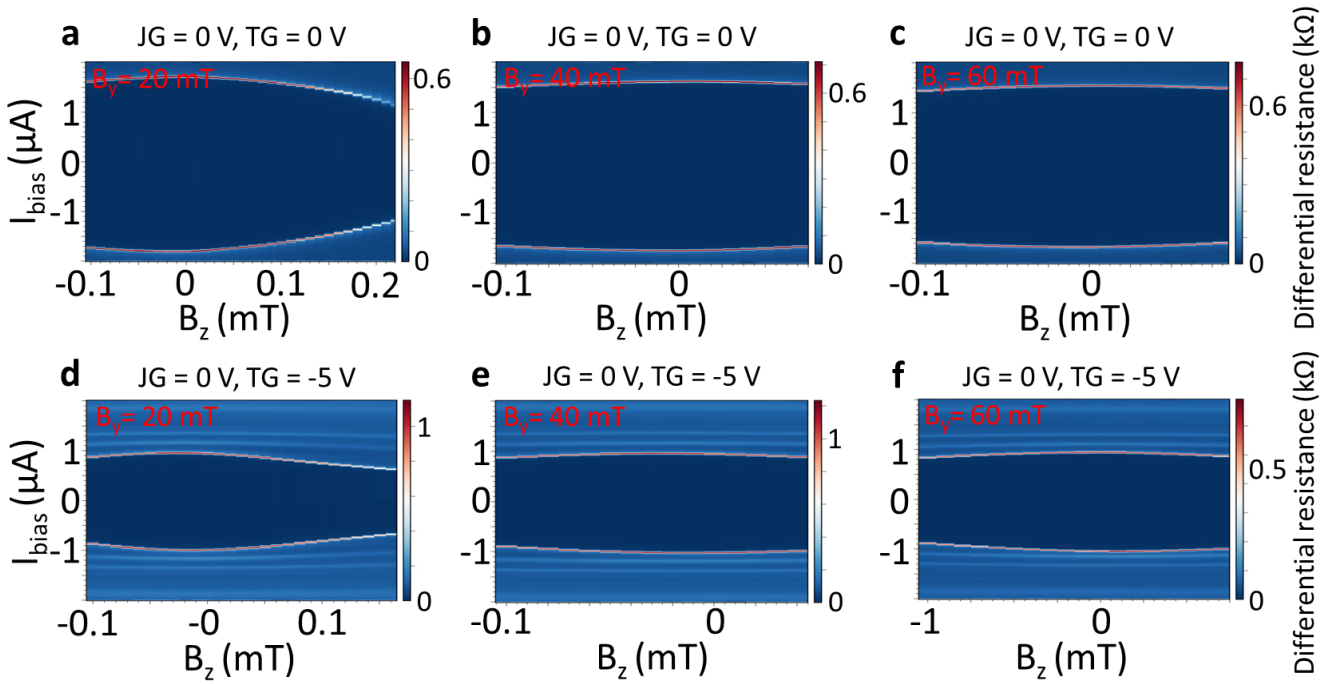

Fig S2. **Fraunhofer patterns at low in-plane field for field alignment.** Here we present B_z scans at different gate voltages that are used to properly align the in-plane fields.

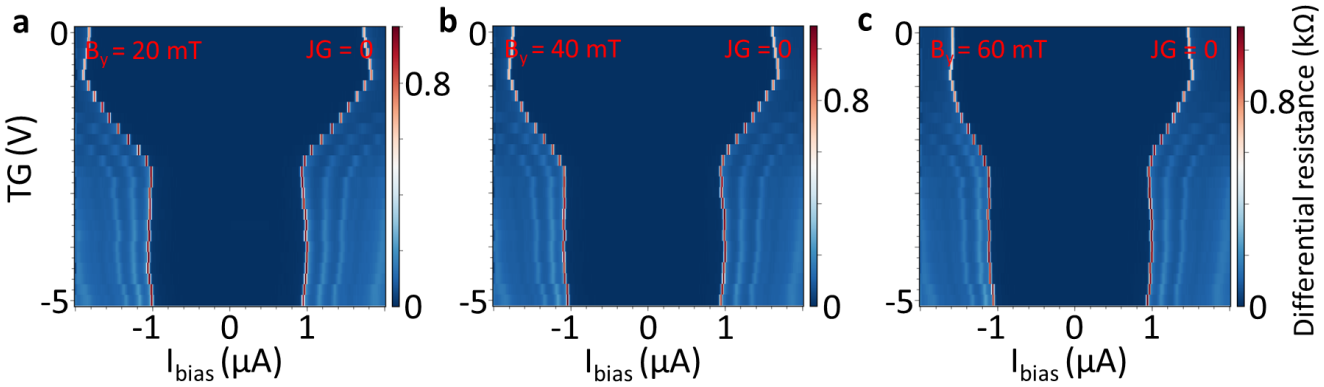

Fig S3. **Bias vs TG scans at low in-plane fields.** Here we present bias vs TG scans at low in-plane fields, from which we extracted the critical current.

of the magnetic field don't alter the qualitative trend. So it is justified that we use zero SOC for simplicity.

In the simplified two-strip structure without SOC or E_z, we see that the general trend can be well captured by the first energy band, see Fig. S13. Therefore, we can shrink the width in the $y-$direction and focus only on the single subband case. The corresponding energy spectrum and current-phase relation show similar behavior to the punched-hole case, when μ_h is decreased, see Fig. S14.

Now to understand the dependence of the supercurrent behavior on the two-strip distance in the simplified structure (see Fig. S13), we calculate the reflection matrix at the interface between the middle superconductor and the right normal strip. The property of this interface is important since the phase jump φ is across the normal strip. To do this, we leave out the right superconductor, and make the normal strip and the left superconductor semi-infinite, see the schematic in Fig. S15(a). The incoming electron mode (denoted by black arrow) is assumed to have amplitude one, and we assume the outgoing wavefunction consists of electron mode (denoted by right-pointing black arrow) and hole mode (right-pointing white arrow). Their amplitudes then give the normal reflection r_N and Andreev reflection

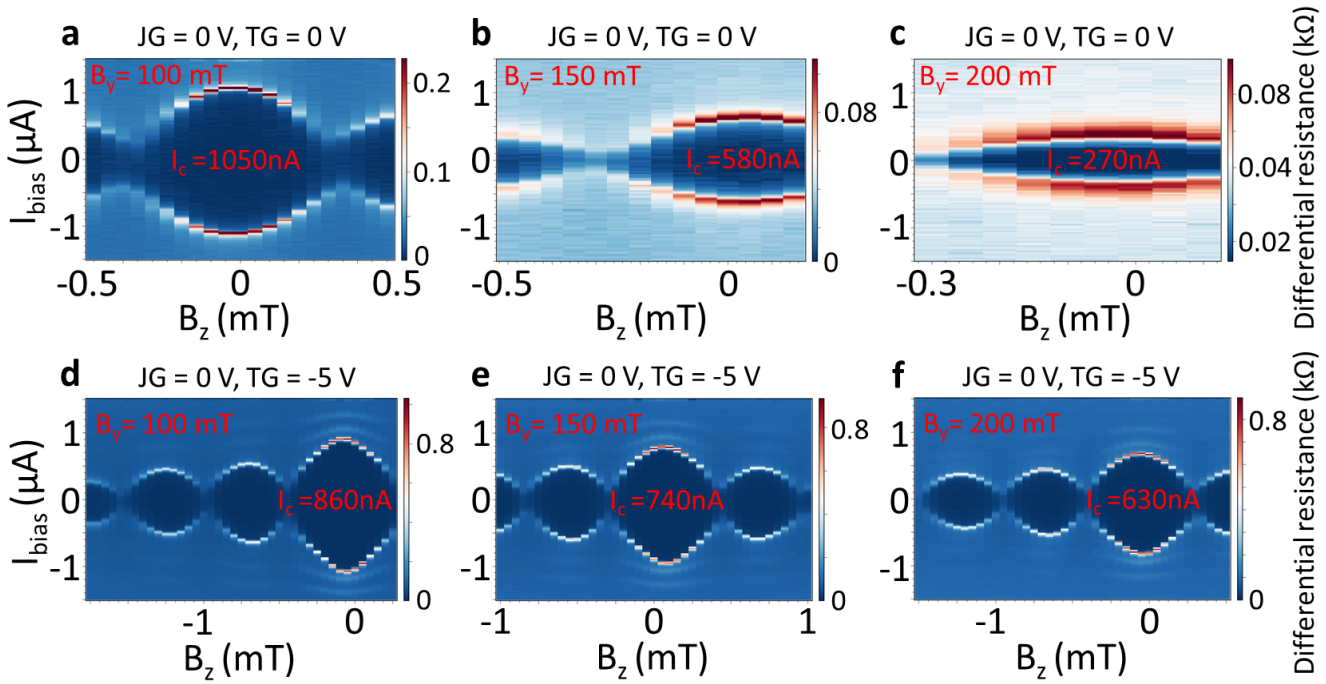

Fig S4. **Fraunhofer patterns at different B_y for different TG voltages.** (a) - (c) Differential resistance as a function of bias current and B_z at B_y = 100 mT, 150 mT and 200 mT for JG = 0 V and TG = 0 V. (d) - (f) Differential resistance as a function of bias current and B_z at B_y = 100 mT, 150 mT and 200 mT for JG = 0 V and TG = -5 V. Maximum switching current I_c is measured at the center of the main lobe.

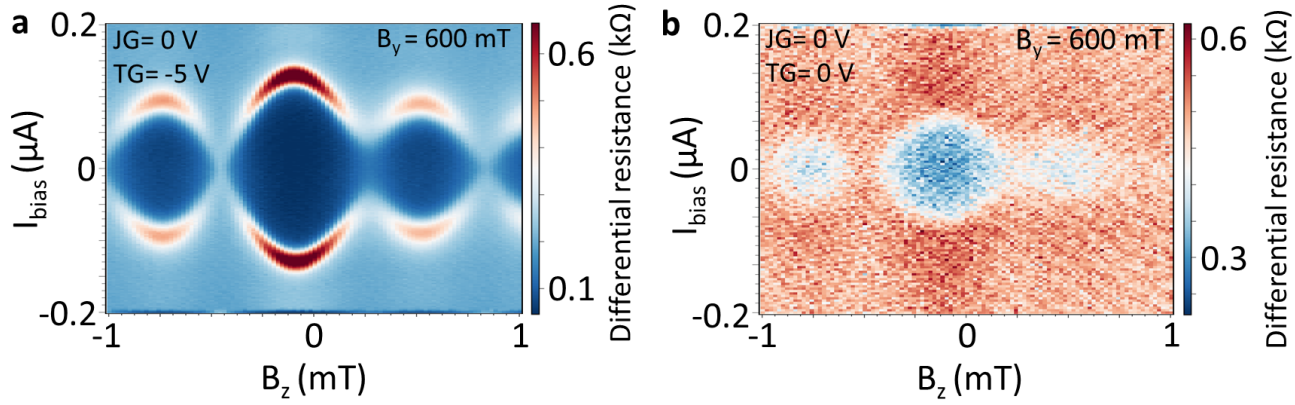

Fig S5. **Fraunhofer patterns at high in-plane fields.** (a) Differential resistance as a function of bias current and B_z at B_y = 600 mT and TG = -5 V. Supercurrent in the main lobe shows around 50 Ω resistance. (b) Differential resistance as a function of bias current and B_z at B_y = 600 mT and TG = 0. Fraunhofer patterns show significant finite resistance.

r_A coefficients, respectively.

Since we are studying the case without magnetic field or SOC, and the Fermi energy we use is close to the band

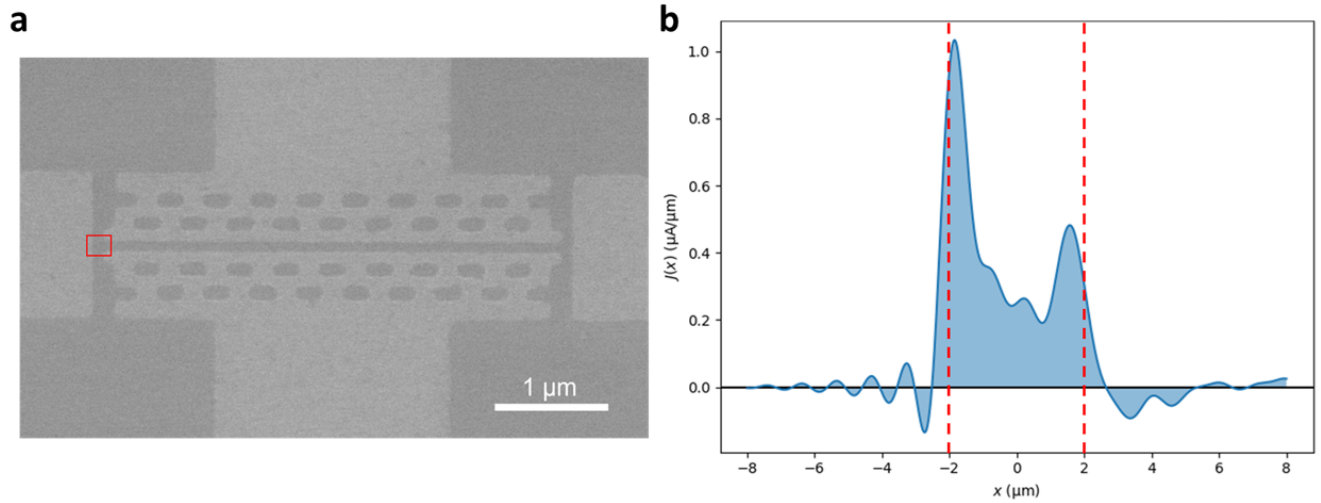

Fig S6. **High supercurrent density at the ends of the junction.** (a) Full SEM image of the device showing the extra Al contacts. (b) Calculated supercurrent density distribution based on Fraunhofer patterns in Fig.1(c). Red dashed lines indicate the Josephson junction edge.

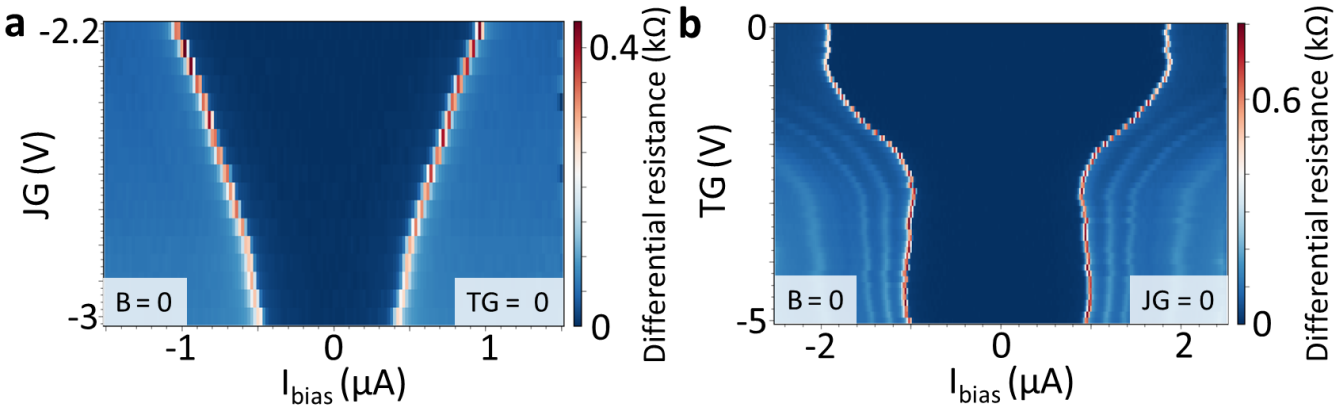

Fig S7. **Hysteresis in current-voltage characteristics.** We observed hysteresis in current-voltage characteristics when the current bias is swept in one direction. (a) Differential resistance as a function of bias current and JG at $B_y = 0$ and TG = 0 with bias swept from positive to negative. (b) Differential resistance as a function of bias current and TG at $B_y = 0$ and JG = 0 with bias swept from positive to negative.

bottom ($\mu \ll t$), the Hamiltonian Eq. (S1) in the momentum space is then simplified to

$$\begin{aligned} H_N &= \sum_{\mathbf{k},\alpha,\beta} \left[4t - 2t\cos(k_x a) - 2t\cos(k_y a) - \mu\right] c^\dagger_{\mathbf{k},\alpha} \left(\tau_{z0}\right)_{\alpha,\beta} c_{\mathbf{k},\beta} \\ &\approx \sum_{\mathbf{k},\alpha,\beta} \left[t\, k^2 a^2 - \mu\right] c^\dagger_{\mathbf{k},\alpha} \left(\tau_{z0}\right)_{\alpha,\beta} c_{\mathbf{k},\beta} \end{aligned} \tag{S4}$$

where $\mathbf{k} = (k_x, k_y)$ and $ka \ll 1$. We obtain a quadratic dispersion $\sim \hbar^2 k^2/2m^*$ where m^* is the effective mass and $t = \hbar^2/2m^* a^2$. Similarly, we have this Hamiltonian in the depleted region and superconductors as well, differing only by the chemical potential or the superconductor pairing gap.

We can then assume the entire wavefunction is in the same spin configuration. The wavefunction is then reduced to two degrees of freedom (electron and hole). In the right normal metal, the wavefunction is

$$\psi = (1,0)e^{-ik_e x} + r_N(1,0)e^{ik_e x} + r_A\sqrt{k_e/k_h}(0,1)e^{-ik_h x} \tag{S5}$$

at energy E, where r_N is the normal reflection coefficient, and r_A is the Andreev reflection amplitude. The electron/hole wavevector is given by $k_{e,h} = \sqrt{2m^*(\mu \pm E)/\hbar^2}$. For the middle superconducting strip, its finite width

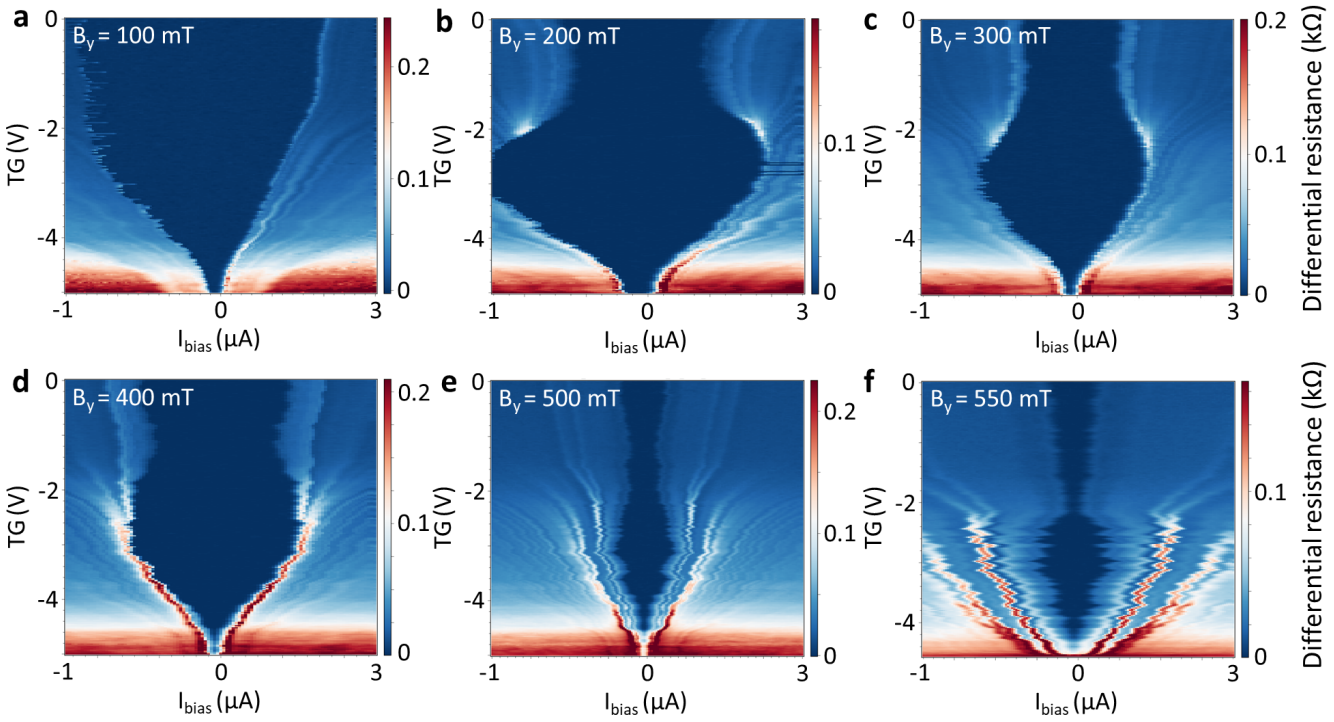

Fig S8. **Enhancement of supercurrent at finite fields in device B.** In device B with the same geometry, enhanced supercurrent can be observed at finite fields when TG depletes (TG < -2 V) the 2DEG in the holes (b-g). In this device, JG is misaligned with the junction, so TG can also tune the chemical potential in the junction and fully deplete the supercurrent. Note that the bias current is swept from positive to negative in these scans.

allows overlap of four modes (decaying in different directions):

$$\begin{aligned}\psi =& C_1(1,e^{i\theta})e^{\lambda x+ik_s x}+C_2(1,e^{-i\theta})e^{\lambda x-ik_s x}\\ &+C_3(1,e^{-i\theta})e^{-\lambda x+ik_s x}+C_4(1,e^{i\theta})e^{-\lambda x-ik_s x}\end{aligned} \tag{S6}$$

where $\cos\theta = E/\Delta$. k_s, λ are non-negative and $k_s + i\lambda = \sqrt{2m^*(\mu + i\Delta\sin\theta)/\hbar^2}$. The wavefunction in the depleted strip (green) is

$$\begin{aligned}\psi =& D_1(1,0)e^{ik'_e x}+D_2(1,0)e^{-ik'_e x}\\ &+D_3(0,1)e^{ik'_h x}+D_4(0,1)e^{-ik'_h x}\end{aligned} \tag{S7}$$

where the electron/hole wavevector in the depleted strip is $k'_{e,h} = \sqrt{2m^*(\mu_h \pm E)/\hbar^2}$.

In the left superconductor, things are simple. There are only two vanishing modes:

$$\psi = E_1(1,e^{i\theta})e^{\lambda x+ik_s x}+E_2(1,e^{-i\theta})e^{\lambda x-ik_s x} \tag{S8}$$

By matching the boundary conditions (both wavefunction ψ and its gradient $\partial\psi/\partial x$) at all interfaces, we can then solve for the coefficients, achieve the reflection matrix, and reconstruct the wavefunction profile in the entire region at $E = 0$. Plugging in the parameter values mentioned before where $a = \xi/6, t = \hbar^2/2m^*a^2 = 7.32\Delta$, $\mu = 1.25\Delta$, and $l_3 = \xi/2$, we then arrive at results shown in Fig. S15. One can see that the strength of the Andreev reflection depends on the depletion potential, in a similar manner to the supercurrent. It reveals that the supercurrent enhancement at certain depletion strength is due to the enhanced Andreev reflection at this point.

If we look at the wavefunction distribution in the depleted strip and middle superconductor, we would see that increasing the depletion strength is always pushing the particle distribution more to the right side of the middle superconductor. An intuitive way to describe the situation might be to look at it as analogous to a "bullwhip effect" in which a downward motion of the handle causes an upward motion of the whip's tail. In this analogy the region

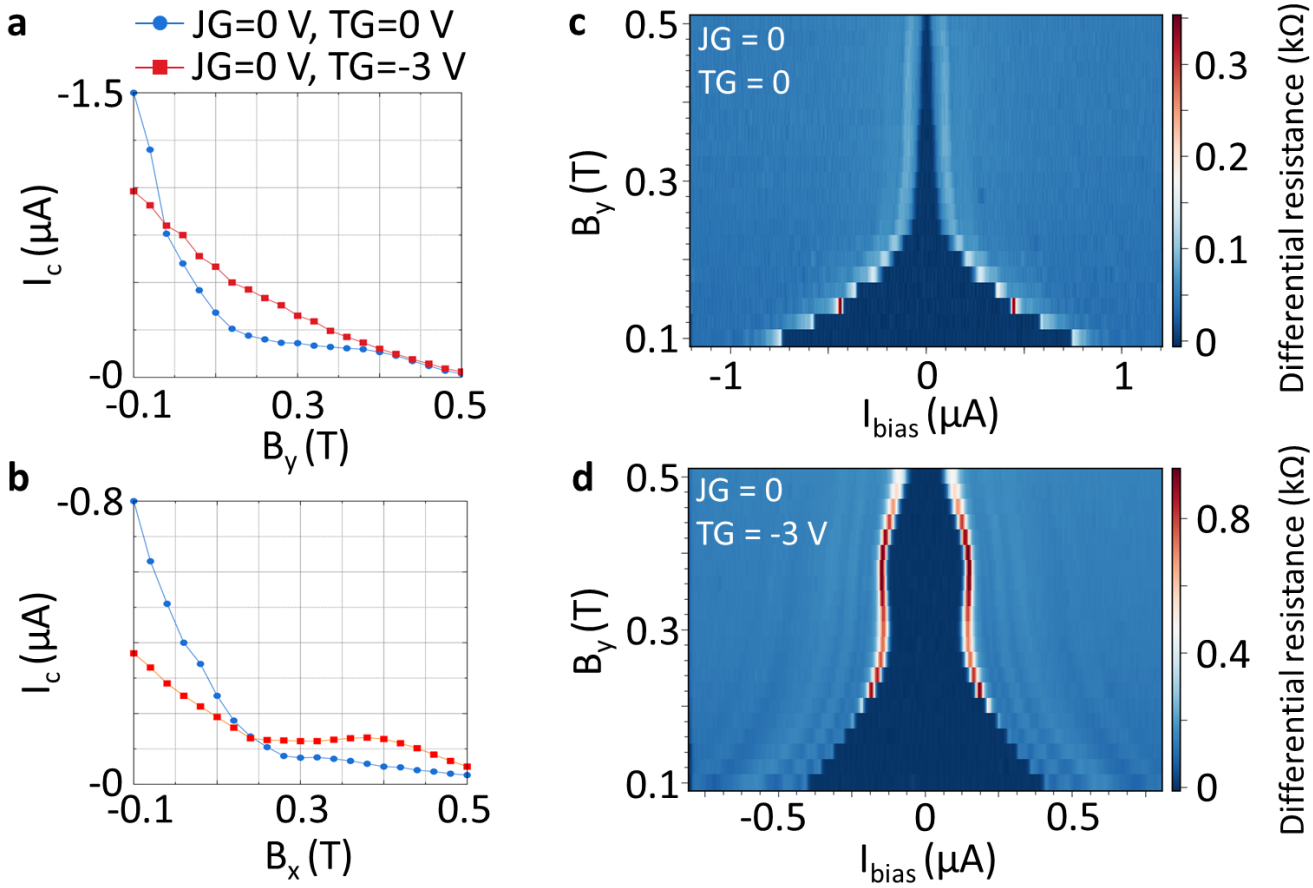

Fig S9. **Supercurrent in-plane field dependence for different gate configurations in device B.** (a) Switching current as functions of B_y for depleted holes (TG = -3 V) and non-depleted holes (TG = 0). (b) Switching current as functions of B_x for depleted holes and non-depleted holes. (c) Differential resistance as functions of bias current and B_y for non-depleted holes. (d) Differential resistance as functions of bias current and B_y for depleted holes. Note bias is swept from positive to negative in panels (c) and (d). Note that the bias current is swept from positive to negative in these scans.

under the holes is the whip's handle: a suppression of the carrier density and therefore of the electron's wavefunction ψ_e under the holes induces an increase of ψ_e in whip's tail, the superconducting section closest to the JJ's normal region. The Andreev reflection is always maximum when the amplitude of the electron sector (denoted as ψ_e) is close to one at the superconductor/normal interface (defined as $x = 0$ position here). When the strip distance is short, $|\psi_e|$ is big (> 1) at the interface without depletion, so stronger depletion is adding the amplitude further, which then decreases $|r_A|$. When the strip distance is increased, there is more space in the middle superconductor, and the electrons spread more towards the left side. The amplitude at $x = 0$ is small without depletion. Now, at a proper depletion, the amplitude gets close to one and $|r_A|$ is optimal. At even larger strip distance, the depletion potential needs to be stronger to increase the electron amplitude at $x = 0$. Within our parameter range of μ_h, $|\psi_e|$ is always smaller than one, and therefore $|r_A|$ is always increasing with $(-\mu_h)$. The corresponding profiles of the quasiparticle current density are provided in Fig. S16 at $l_2 = \xi/6, \xi/2$ without magnetic fields.

---

[1] The qualitative picture is always the same as long as g_{sc} doesn't vanish, independent of the detailed value.

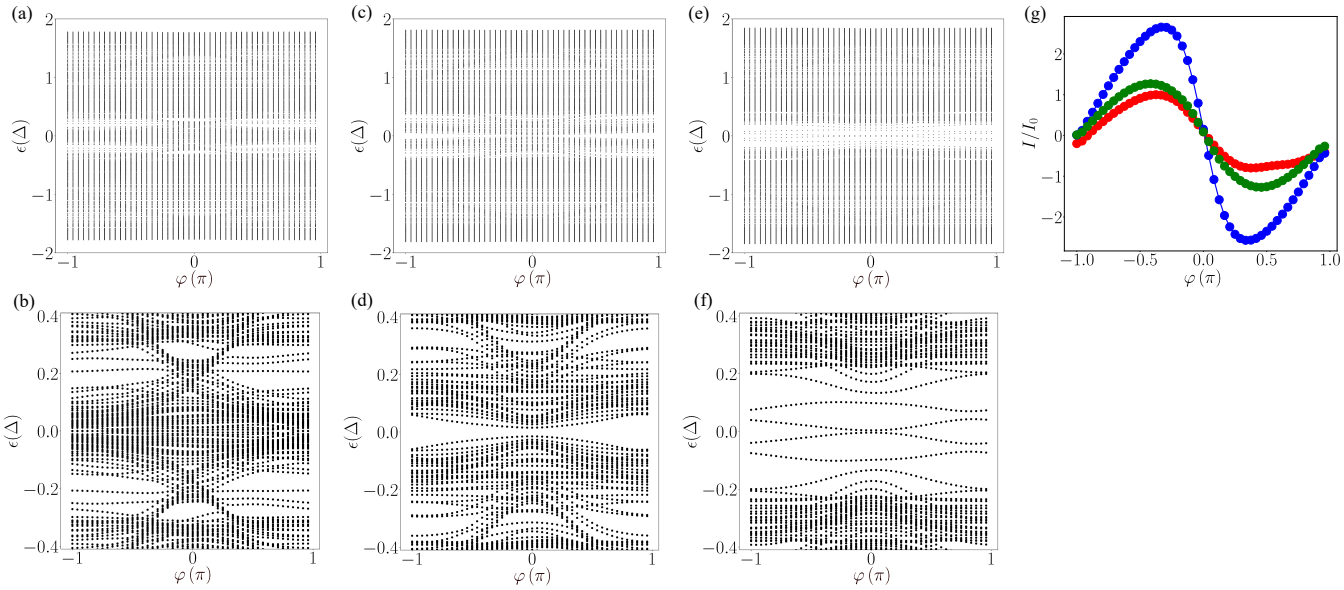

Fig S10. (a) and (b), (c) and (d), (e) and (f) are full and zoomed-in view ABSs' spectra as a function of the phase difference ϕ, corresponding to N1, N2, N3 in Fig. 4(d) respectively. (g) Current-phase relation for N1 (red), N2 (blue), and N3 (green). $I_0 = I_c(\mu_h = \mu)$.

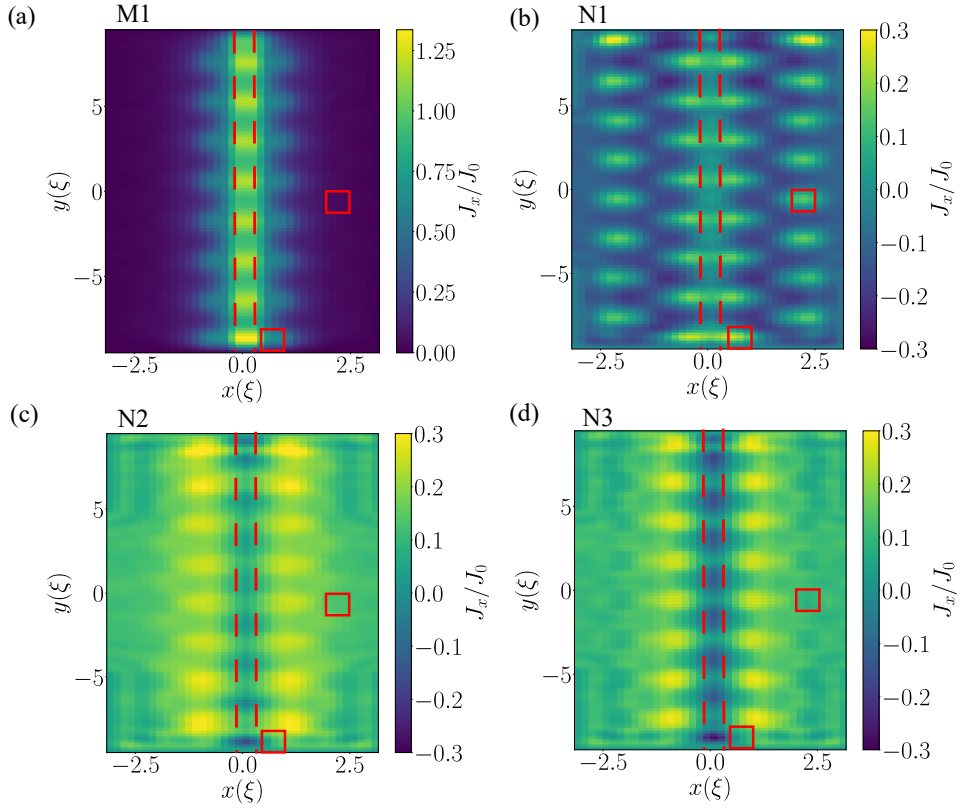

Fig S11. (a) Profile of J_x for the case when $E_Z = 0$ and $\mu_h = \mu$, M1 point in Fig. 4 (c). (b), (c), (d) Profiles of J_x for the case when $E_Z = 1.14\Delta$ and μ_h corresponds to the points N1, N2, N3 in Fig. 4 (d), respectively. J_0 is the average current density for the case when $E_Z = 0$, $\mu_h = \mu$. The red dashed lines indicate the boundary of the normal strip. The red boxes show positions of some of the depleted holes.

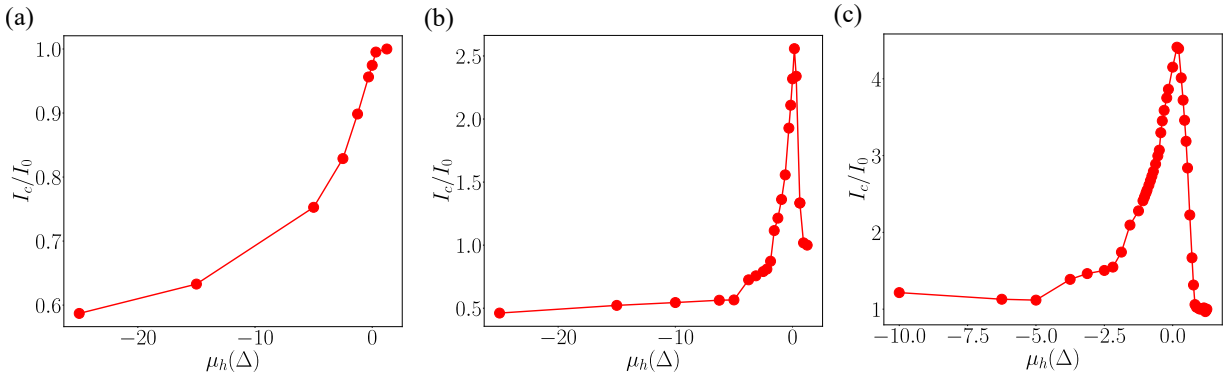

Fig S12. (a) I_c vs μ_h at $E_z = 0$ without SOC in the punched-hole setup. (b) I_c vs μ_h at $E_z = 1.14\Delta$ without SOC in the punched-hole setup. (c) I_c vs μ_h at $E_z = 1.14\Delta$ when the magnetic field is along the $x-$direction with SOC in the punched-hole setup. $I_0 = I_c(\mu_h = \mu)$.

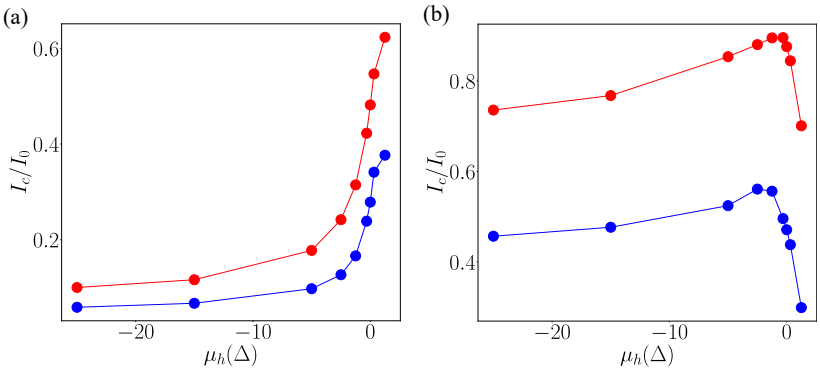

Fig S13. (a) I_c vs μ_h in the simplified two-strip setup at $l_2 = \xi/6$. (b) I_c vs μ_h in the two-strip setup at $l_2 = \xi/2$. Supercurrents are scaled by $I_0 = I_c(\mu_h = \mu)$ and divided to contribution from the first band (red) and the rest bands (blue).

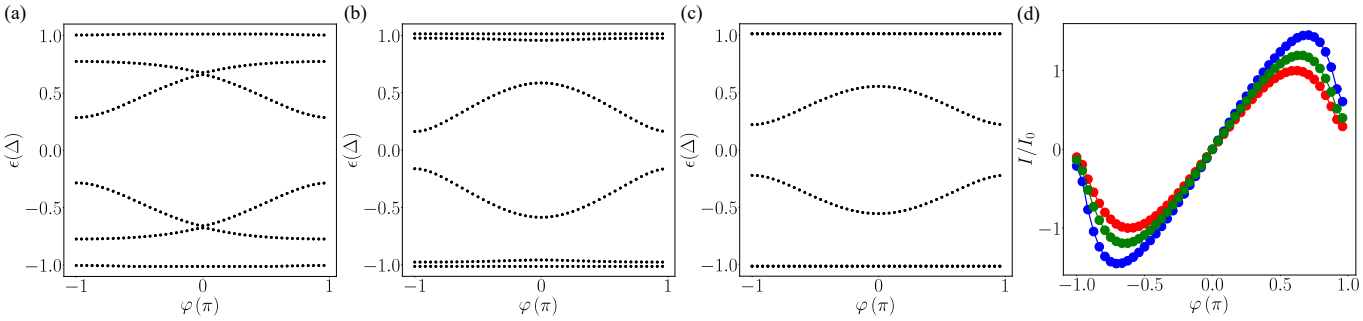

Fig S14. (a)-(c) Energy spectrum ϵ vs phase difference ϕ in the two-strip setup at $l_2 = \xi/2$, corresponding to $\mu_h = \mu$, -1.25Δ, and -25Δ, respectively. (d) Current-phase relation at $\mu_h = \mu$ (red), -1.25Δ (blue), and -25Δ (green). $I_0 = I_c(\mu_h = \mu)$.

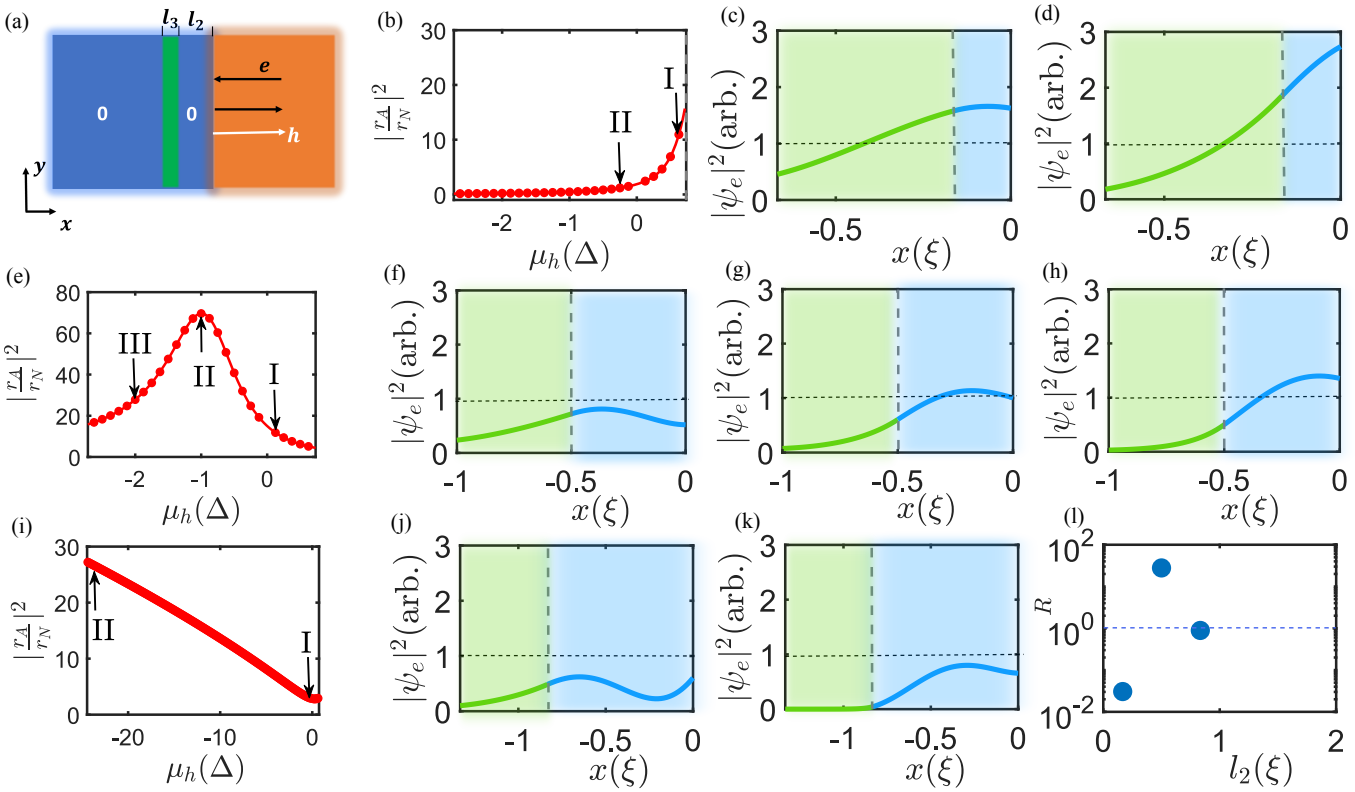

Fig S15. (a) Setup for calculation of the reflection matrix. The phases are assumed zero for the left and middle superconductors. Here we focus on the $x-$direction degree of freedom. (b) $|r_A/r_N|^2$ at $l_2 = \xi/6$. (c) and (d) Distribution of electron density in the depleted strip (green) and middle superconductor (blue) $|\psi_e(x)|^2$, corresponding to points I and II in the (b) panel. (e) $|r_A/r_N|^2$ at $l_2 = \xi/2$. (f)-(h) $|\psi_e(x)|^2$ at I, II, and III of the (e) panel. (i) $|r_A/r_N|^2$ at $l_2 = 5\xi/6$. Due to the large distance and weak coupling between the two strips in this case, the effect of the depletion is much weaker and therefore we examine a larger range of μ_h. (j) and (k) $|\psi_e(x)|^2$ at I and II of (i) Panel. (l) Relative Andreev reflection strength $R = |r_A/r_N|^2/R_0$ at $\mu_h = -\Delta$ as a function of strip distance l_2. Here R_0 is the value of $|r_A/r_N|^2$ without depletion for each l_2 choice.

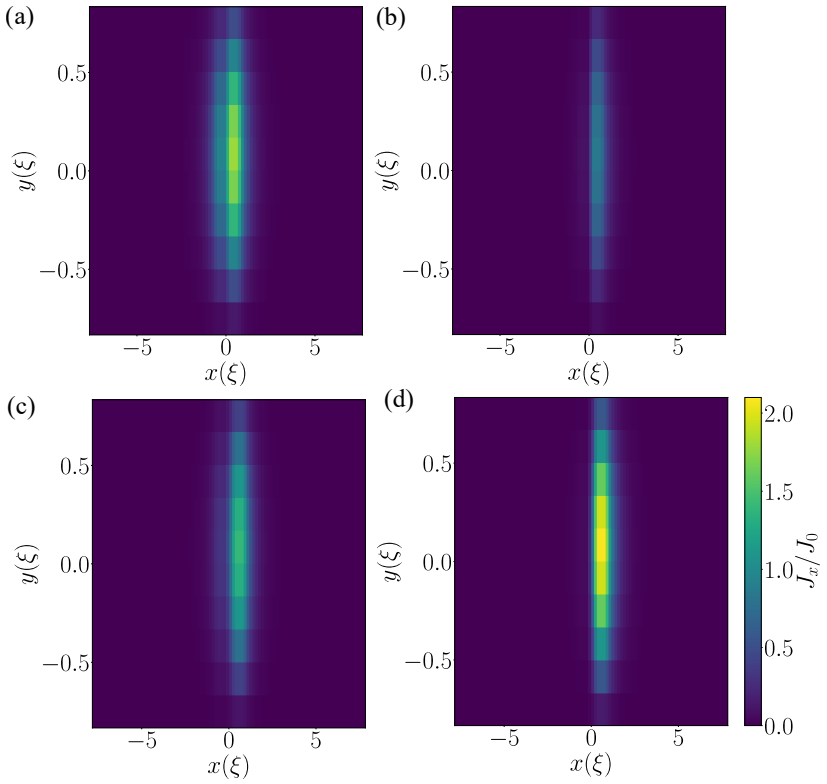

Fig S16. (a) and (b) Quasiparticle current density $J_x(x, y)$ for $l_2 = \xi/6$, at $\mu_h = \mu$ and $\mu = -1.25\Delta$, respectively. (c) and (d) $J_x(x, y)$ for $l_2 = \xi/2$, at $\mu_h = \mu$ and $\mu_h = -1.25\Delta$. J_0 is the average current density at $l_2 = \xi/6$, $\mu_h = \mu$. All plots share the same color bar.